INTERFACE

Research

Author for correspondence:
Jie Xiao
e-mail: jie.xiao@suda.edu.cn

How eyelashes can protect the eye through inhibiting ocular water evaporation: a chemical engineering perspective

Siyu Zou, Jinping Zha, Jie Xiao and Xiao Dong Chen

School of Chemical and Environmental Engineering, College of Chemistry, Chemical Engineering and Materials Science, Soochow University, Suzhou City, Jiangsu Province 215123, People's Republic of China

SZ, 0000-0002-9152-9844; JX, 0000-0001-7842-7862

Bionics is a fascinating subject that has inspired many inventions through learning from biological structures and functions. In this work, a coupled multi-physics model has been developed to characterize ocular water evaporation with realistic eyelash structures taken into account. From a chemical engineering perspective, the protective function of human eyelashes in terms of evaporation inhibition has been rationally revealed. Systematic investigations were carried out to elucidate the effects of different eyelash lengths, orientations and inlet air directions on water evaporation on the ocular surface. The results clearly demonstrate that regardless of inlet air directions and eyelash orientations, increasing eyelash length from zero to an optimal length can effectively reduce water evaporation. However, further increase in the eyelash length can lead to enhanced evaporation. For the normal and parallel inlet air directions, the optimal eyelash length is around 15–30% of the eye width and can offer approximately 10–30% evaporation reduction when compared with the cases without eyelashes. These values are independent of the eyelash orientation. This investigation provides valuable data for in-depth understanding of the protective function of the eyelashes, which can be used in the future to improve and optimize bionic designs inspired by human eyelashes.

1. Introduction

Biology is a rich source for all kinds of technical ideas, engineering principles and major inventions of mankind. In the second half of the twentieth century, the development of bionics had stimulated great interests on the study of biological functions. Nowadays, bionics are widely used to bridge biology and technology for the innovative design of industrial facilities [1–6] (table 1).

Interesting research based on human eyelashes has been performed. Mammal eyelashes are the typical results of natural selection and its length, orientation, quantity and other parameters seem to follow a certain selection law. Its protective functions, however, are not yet fully understood. Eyelashes are a hair structure which is very common for mammals and similar structures can also be found in birds and reptiles. Generally, as a product of biological evolution, eyelashes have different structures and functions for animals living in different environments [7]. Eyelashes are delicate and sensitive sensors that can help the creature to avoid the threat of foreign objects to the eyes [8]. It can provide a warning signal when eyes are exposed to the external stimulus, which directly leads to eye blinking. Eyelashes are also known as filters or sunshades that can help animals to adapt to the living environment [9]. For example, camels, giraffes and ostriches living in dry and dusty areas with strong sunlight have unique, multi-layered thick eyelashes, which help them filter the dust in the air and shield the strong sunlight. However, pets such as cats that are far away from these environments have almost no eyelashes. Furthermore, eyelashes as a human facial detail can capture the attention of others [10]. Obviously, eyelash loss or abnormal growth of eyelashes can

THE ROYAL SOCIETY
PUBLISHING

Table 1. Nomenclature.

c	vapour concentration in moist air (mol m^{-3})
C_p	specific heat capacity of the moist air (J/(kg K))
D	vapour diffusivity (m^2 s^{-1})
k	thermal conductive of the moist air (W/(m K))
L	length of eyelashes (m)
p	pressure (Pa)
p_v	vapour pressure of the moist air (Pa)
p_{sat}	saturated vapour pressure of the moist air (Pa)
p'_{sat}	saturated vapour pressure in kilopascals (kPa)
R	ideal gas constant (J/(mol K))
t	time (s)
T	temperature (K)
T_c	temperature in degrees Celsius (℃)
$\boldsymbol{u}$	velocity vector (m)
W_x	width of palpebral fissure (m)
W_y	height of palpebral fissure (m)
L_{top}	length of top eyelashes (m)
L_{bot}	length of bottom eyelashes (m)
Greek letters	
ρ	density (kg m^{-3})
μ	viscosity (Pa s)
ϕ	relative humidity of the moist air

affect these functions, and is even associated with the development of some diseases [11,12].

Another important function deserving further investigation is the inhibition of ocular water evaporation since a moist ocular surface is critical for the health of eyes. To quantitatively understand ocular water evaporation is not an easy task because it involves multiple coupled transport phenomena occurring adjacent to the eye. The effects of mammal eyelash lengths on ocular water evaporation were investigated by Amador *et al.* [7] through experiments, scaling theory and numerical simulations. Their results revealed that the eyelashes have an optimal length, at which the ocular surface has the lowest water evaporation rate. The functions of hairy eyes found on insects have also been revealed using a similar approach [13], suggesting that when the hair length of hairy eyes is almost equal to hair spacing, a thicker velocity boundary layer can be formed when compared with the smooth, hairless eyes. This simple mechanism prevents particle deposition on the ocular surface.

However, biological or medical experiments are generally difficult to carry out for the *in vivo* study of human or mammals eyelashes because of the constraints on medical ethics and animal protection policies. Also, bionic experiments may not be able to reproduce the real biological system due to limitation on experimental techniques. Now, with ever-increasing computer performance, the multi-physics modelling and simulation have been widely used to investigate various complex biological systems due to its advantages of low cost and flexibility. Numerical simulation as an effective method was applied to the investigation of coupled transport phenomena in our research. Systematic numerical studies of evaporation on the ocular surface should be more convenient than

experiments and realistic biological structures can be fully taken into account. Although simulation research have been carried out before [7,13], previous studies focused on theoretical analysis for a simplified system and evaporation was not directly predicted. It was assumed that evaporation rate is proportional to the shear rate. Furthermore, the realistic structures of the human eye and eyelashes had not been reproduced in previous studies. Until now, no research has been conducted to directly simulate the water evaporation coupled with momentum and energy transfer between the eye and the surrounding air, and the effects of geometric details of eyelashes on eye protection remain unclear. In this paper, the direct numerical simulation of water evaporation on the ocular surface with more realistic human eye structures have been conducted. This multi-physics numerical model can improve our fundamental understanding of the protective function of human eyelashes.

In the following text, the multi-physics model involving momentum, energy, mass transfer and evaporation is introduced to characterize water evaporation over the ocular surface. By resorting to this model, various eyelash lengths, orientations and inlet air directions were investigated to quantitatively compare how eyelash structures can impact the evaporation process. The optimal eyelash length was then identified. Inhibition or enhancement mechanisms of eyelashes on evaporation have been discussed based on the detailed analysis of comprehensive results. Systematic numerical simulations can hopefully provide some suggestions on future design of eyelash-inspired products, e.g. artificial eyelashes that can additionally keep the ocular surface moist, and the specially designed anti-dry sensor.

## 2. Modelling and simulation method

2.1. System specification

The schematic diagram of the simulated system is shown in figure 1. A sphere is used to represent the eyeball. The ocular surface is in the middle of the surface of the spherical cap, which is surrounded by three layers of evenly distributed eyelashes. The length difference between top and bottom eyelashes has been considered. Specifically, as reported by Thibaut *et al.* [14], top ones are 2 mm longer than the bottom ones in the current study. The eyelashes are simplified as cylinders without curvatures and they are not deformable [7]. The shape of the palpebral fissure can be constructed by projecting an ellipse to the spherical cap. The remaining areas of the surface on the spherical cap are the top and bottom eyelids.

The geometric settings are specified based on the data of real human eyes. All parameters used in our model are listed in table 2. The three-dimensional computational domain of the human eyelash system is a rectangular box with dimensions of $5W_x \times 5W_x \times 4W_x$ (figure 2). Owing to the geometrical symmetry, only half of the ocular surface is used in the computation to simplify the system and reduce computational cost. The evaporation process coupled with airflow, mass and energy transfer have been modelled.

2.2. Governing equations

The air in the room is considered as an incompressible fluid [24] because the volume change does not exceed 5% when the Mach number is much less than 0.3. The eyelashes form a
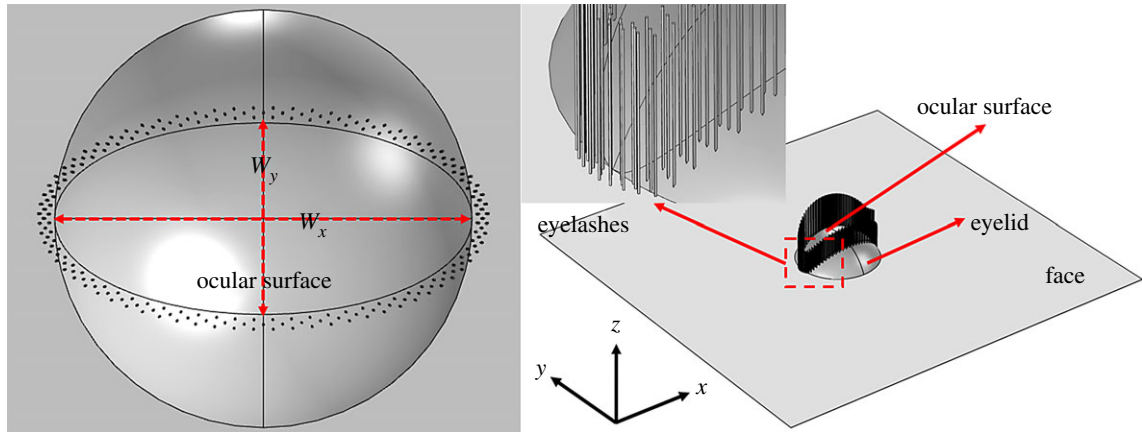
Figure 1. Top and side views of the palpebral fissure, eyelashes and eyelid. (Online version in colour.)
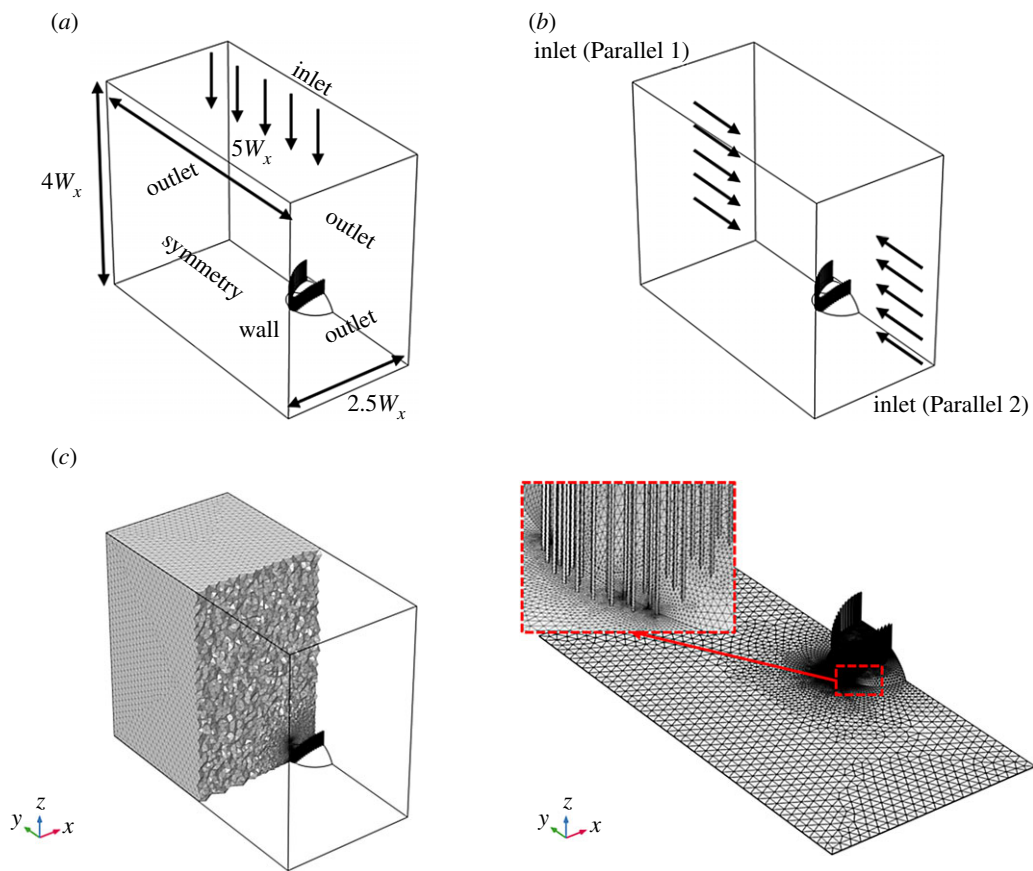
Figure 2. The schematic diagram of the computational domain showing: (*a*) dimensions and boundary conditions for the cases with normal inlet air, (*b*) boundary conditions for the cases with parallel inlet air and (*c*) the mesh, fine meshes can be found on and adjacent to the ocular surface in order to capture sharp gradients of physical quantities. (Online version in colour.)

Table 2. Physiological data of human eye and eyelashes.

parameters	model values	anatomical mean values
width of palpebral fissure (W_x)	22 mm	26–32 mm [15–17]
height of palpebral fissure (W_y)	10 mm	9–10 mm [18,19]
number of eyelashes	108 (uniform distribution)	100–150 (palpebra superior)/50–75 (palpebra inferior) [14]
length of top eyelashes (L_{top})	10 mm	8–12 mm [14,20]
length of bottom eyelashes (L_{bot})	8 mm	6–8 mm [14,20]
diameter of eyelash	100 μm	92.7–97.0 μm [21]
ocular surface temperature	32℃	32.06 ± 1.24℃ [22]
number of eyelash layers	3	5–6 (palpebra superior)/3–4 (palpebra inferior) [14,23]

channel with an elliptical cross-section in our simulations. The length of semi-major axis of this ellipse is $a = W_x/2 = 11$ mm and semi-minor axis is $b = W_y/2 = 5$ mm. The Reynolds number based on the hydraulic diameter of the channel is around 881. Hence, the flow is laminar. The full three-dimensional incompressible Navier–Stokes equations are adopted to simulate the airflow around the eyelashes and ocular surface, the vector form of the Navier–Stokes equation system can be written as

$$\nabla \cdot \boldsymbol{u} = 0 \tag{2.1}$$

and

$$\rho\frac{\partial \boldsymbol{u}}{\partial t} + \rho(\boldsymbol{u} \cdot \nabla)\boldsymbol{u} = -\nabla p + \mu\nabla^2\boldsymbol{u}, \tag{2.2}$$

where ρ is the air density, kg m^{-3}; $\boldsymbol{u}$ is the velocity vector, m s^{-1}; p is fluid pressure, Pa; μ is the air viscosity, Pa s. The fluid density and viscosity are assumed to be independent of fluid temperature and water vapour concentration due to the modest variation range of temperature and vapour concentration.

The human body can be treated as a system with a constant temperature, the temperature of the skin and the ocular surface are kept constant. Direct numerical simulation has been implemented in this work to describe water evaporation. The energy exchange and water vapour transfer between moist air and ocular surfaces are similar, all subjected to the convection–diffusion equation in the fluid system. Note that the velocity in equation's (2.3) and (2.4) should be obtained from momentum equations. Thus, the energy equation and mass transfer equation are coupled with the flow equations by velocity. Also, note that the diffusion coefficient in the mass transfer equation is coupled with temperature in the energy equation to describe the effect of temperature on the water vapour diffusion process. The general form of mass and heat convection–diffusion equations can be written as

$$\frac{\partial c}{\partial t} + \boldsymbol{u} \cdot \nabla c = D\nabla^2 c \tag{2.3}$$

and

$$\rho C_p\frac{\partial T}{\partial t} + \rho C_p \boldsymbol{u} \cdot \nabla T = k\nabla^2 T, \tag{2.4}$$

where c is the vapour concentration in moist air, mol m^{-3}; D denotes vapour diffusivity, m^2 s^{-1}; T denotes the temperature of the moist air, K; C_p is the specific heat capacity of the moist air, J/(kg K), k is the thermal conductive of the moist air, W/(m K).

In order to describe the process of water evaporation on the ocular surface, evaporation models are required. In our model, the ocular surface is assumed to be always wet and is covered by a layer of saturated vapour of water, which drives vapour transport from the ocular surface to the ambient air with lower vapour concentration. The vapour concentration in the system can be calculated with the ideal gas equation of state, associated with local temperature and vapour pressure of the moist air [25], which is defined as follows:

$$c = \frac{p_v}{RT}, \tag{2.5}$$

where R is the ideal gas constant, J/(mol K); p_v is the vapour pressure (Pa) of moist air and is related to air humidity, ϕ, as

$$\phi = \frac{p_v}{p_{\text{sat}}}, \tag{2.6}$$

Table 3. Boundary conditions and initial conditions for the base case.

variables	value	units
inlet velocity	1	m s^{-1}
inlet temperature	25	°C
inlet humidity	0.5	—
ocular surface temperature	32	°C
ocular surface humidity	1	—
outlet pressure	1	atm
initial temperature	25	°C
initial humidity	0.5	—

where p_{sat} is the saturated vapour pressure (Pa) and is described by the August–Roche–Magnus equation [26]. Noted that the temperature (T_c) is in degrees Celsius (°C) and the saturation vapour pressure (p'_{sat}) is in kilopascals (kPa) in this equation

$$p'_{\text{sat}} = 0.61094 \exp\left(\frac{17.625 T_c}{T_c + 243.04}\right). \tag{2.7}$$

The vapour diffusion coefficient in the diffusion–convection equation is calculated with an empirical correlation [27]

$$D = 1.963 \times 10^{-7} T - 3.33307 \times 10^{-5}. \tag{2.8}$$

2.3. Initial and boundary conditions
In our model, the air with a constant velocity of v_{in}, ambient humidity of ϕ_{in} and environment temperature of T_{in} flows into the computational domain and impacts on the bottom walls that include the human face, eyeballs and eyelashes (figure 1). No-slip boundary conditions are applied to the walls. The other three side walls are set as pressure outlets which allow the outflow of air. The humidity of the ocular surface is assumed to be equal to 1 due to tear formation by involuntary blinking behaviour. The temperature of the ocular surface and face is set to 32°C. At the symmetry plane of the computational domain, the symmetry boundary condition is specified for momentum, energy and mass transfer, meaning there is no normal flow and no concentration or temperature flux across this plane. All other walls are set as thermal insulation. The initial temperature of the entire calculation domain is equal to the inlet ambient temperature, and the initial humidity is set to the inlet ambient humidity. All boundary conditions and initial conditions are summarized in table 3.

2.4. Numerical simulation method
In this work, all PDEs were solved at steady state using COMSOL Multiphysics software [28]. These numerical procedures were realized using the finite-element method and iterated to a residual of less than 0.001 to obtain a convergent solution. The momentum equation was solved first to obtain the velocity field. The velocity was then used in the energy and mass transfer equations, which were solved together to get temperature and concentration fields, respectively. Note that diffusivity in the mass transfer equation is a function of temperature (see equation (2.8)). After solving the coupled equations using the stationary solver, the detailed spatial
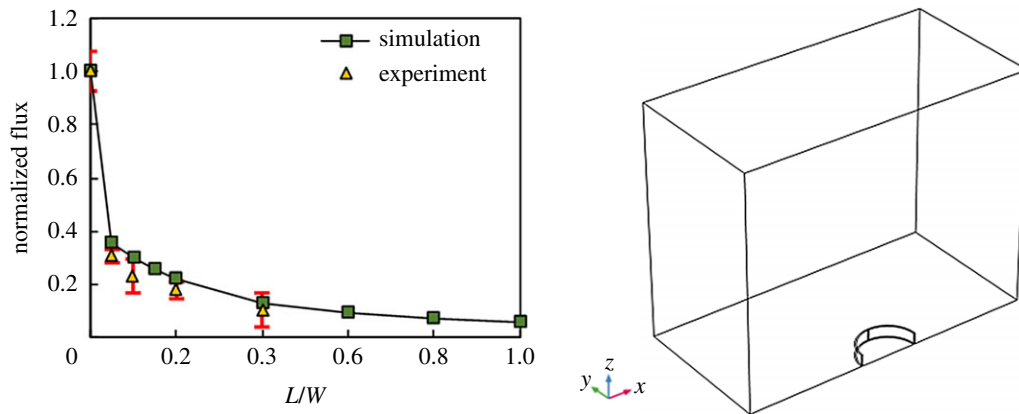
Figure 3. Evaporation flux as a function of impermeable wall height (comparison between experimental data and model predictions). (Online version in colour.)

distributions of velocity, vapour concentration, temperature of moist air and other information in the complete computation domain can be obtained and analysed.

The generated mesh for the calculations has millions of free tetrahedral computational cells with two boundary layers on the no-slip walls to capture the sharp gradients of momentum, temperature and vapour concentration. All boundary layers have prism layer elements and with 20% increase in thickness per layer in the normal direction. Closer to the ocular surface, extreme fine meshes are used to capture gradients and guarantee the accuracy of the calculation. The maximum element growth rate of 1.15 is adopted for the domain away from the ocular surface in order to reduce mesh density and computational cost. The typical mesh structures are presented in figure 2.

In order to identify the mesh resolution that can produce accurate predictions with sufficiently high computational efficiency, a study on mesh independence was carried out. Four meshes consisting of 3.08, 3.63, 4.08 and 4.56 million cells were tested. The mesh density of the bulk area above the ocular surface almost remains constant, but the ocular surface mesh is refined successively. The independence results will be discussed later.

2.5. Model validation

In order to verify the accuracy of this approach, a series of numerical validations were performed and compared with experiments by Amador *et al.* [7]. In the experiments, a small wind tunnel system was designed to test the amount of water evaporation on the eyeball surface at certain wind speeds.

In this study, two sets of experiments are used to test the accuracy of the model. In experiment 1, water evaporation on mimetic ocular is measured when there is no airflow; experiment 2 measures water evaporation on the mimetic ocular surface under different impermeable wall heights and a constant wind speed. The computational domain and geometrical details used in the numerical simulation are the same as the experiments (figure 3). The boundary and initial conditions are consistent with the experiments. Air flows into the computational domain with a constant velocity of $0.365 \, \text{m s}^{-1}$. The temperature of entrance and mimetic ocular are subjected to local room temperature in experimental conditions, which is $T = 21.5°C$. At the ocular surface, the relative humidity is $\phi_{eye} = 1$. The initial humidity of air is set to $\phi_{air} = 0.46$. The initial temperature of air is equal to $T = 21.5°C$. Moreover, it is assumed that the experiments have been done to

reach steady-state conditions due to the long experimental time (10 min for each test).

In the first validation case, the predicted evaporation rate is $2.58 \times 10^{-7} \, \text{mol s}^{-1}$, which is very close to the experimental data of $2.67 \times 10^{-7} \, \text{mol s}^{-1}$. The prediction deviation is only about 3.3%. For the second round of validation, the predicted evaporation rates are compared with the experimental data (figure 3). The same trend can be observed and the deviation is less than 5% deviation. It can be concluded that this numerical model has sufficient accuracy to describe this complex multi-physics coupled phenomenon.

3. Results and discussion

The analyses in this section are based on comprehensive data on three-dimensional distributions of flow, vapour concentration and temperature inside the computational domain. In-depth understanding of the protective mechanisms of eyelashes is discussed.

3.1. Base-cases analysis

The mesh independence study for case 1 is addressed first (see parameter settings in tables 2–4). The evaporation flux and shear rate along a cutline at the ocular surface are plotted in figure 4. Trivial variation of evaporation flux and shear rate for all four meshes can be identified. Mesh 3 is applied to all subsequent simulations.

As demonstrated in figure 2, two cases with two extreme inlet air directions are designed in the current study: case 1 has vertical inlet air (i.e. normal to the ocular surface) and case 2 has horizontal inlet air (i.e. parallel to the ocular surface). Noted that there are two inlet directions for case 2 due to the different lengths between the top and bottom eyelashes. The corresponding cases are referred as 'Parallel 1' and 'Parallel 2' in the following text. Two corresponding cases without eyelashes are also studied as control groups. The steady-state solutions of four cases are illustrated in figures 5 and 6. Note that the data ranges are adjusted to be the same in order to facilitate comparison between cases. The velocity magnitude distributions and streamlines are plotted on the symmetric plane of the computational domain, and the concentration distributions are given on the surface with human eyelids, ocular surface and face. The evaporation flux distributions on the ocular surface are also plotted. The inlet flow direction is indicated for both cases by black arrows.
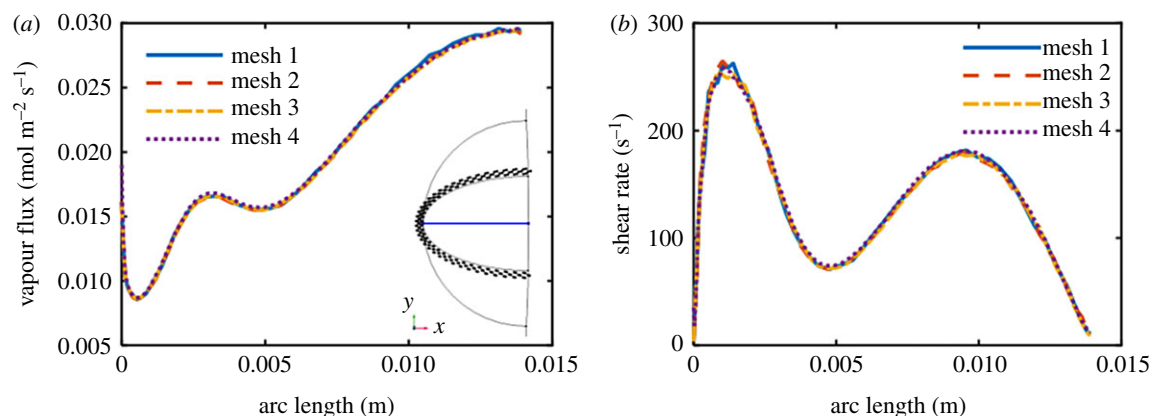
Figure 4. Mesh independence study: (a) the vapour flux along cutline for simulations using different meshes, the central horizontal line on the ocular surface indicates the cutline for results extraction; (b) the shear rate along cutline for simulations using different meshes. (Online version in colour.)
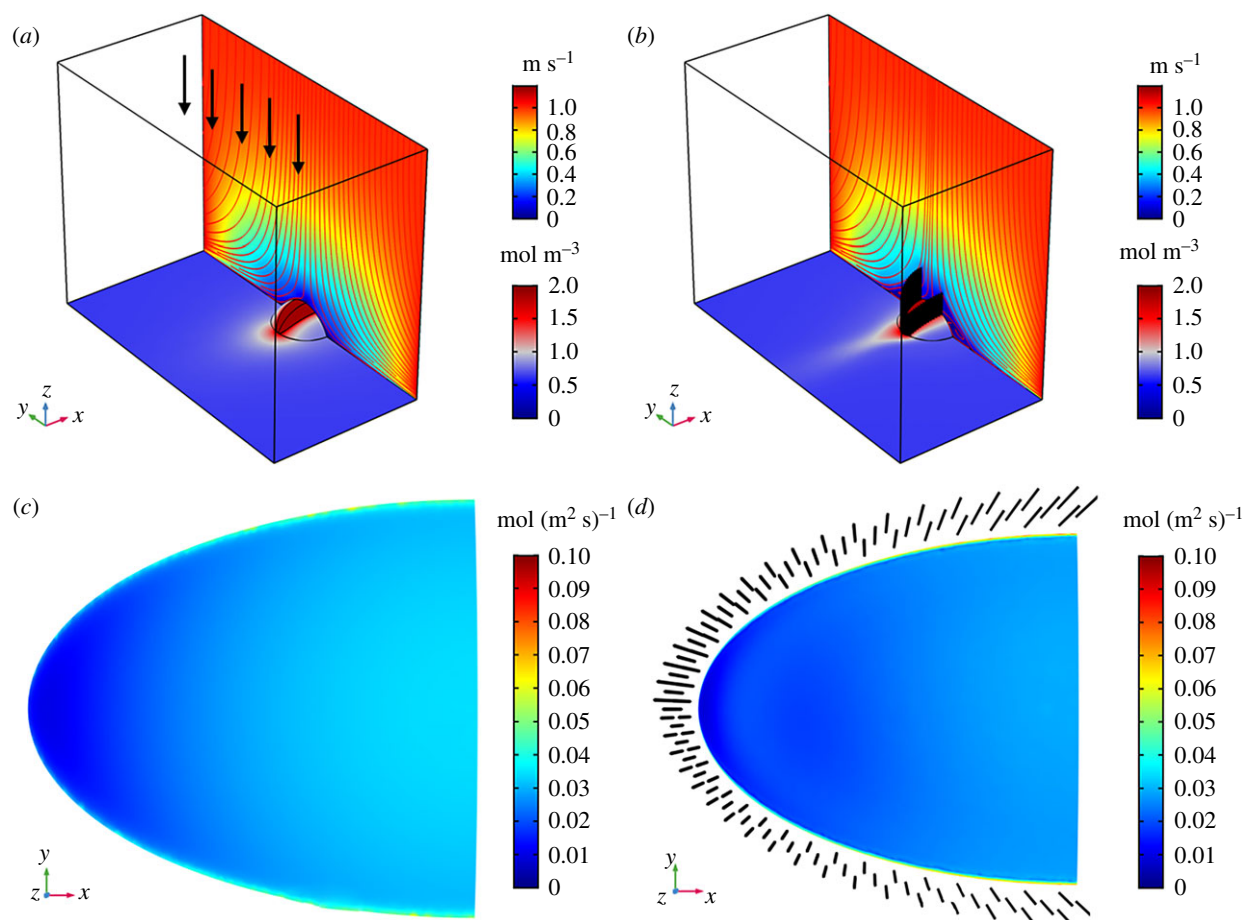
Figure 5. Distributions of physical quantities for the cases with normal inlet air: (a) and (b) are for velocity and vapour concentration distributions; (c) and (d) are for vapour flux distributions on the ocular surface; (a) and (c) are for cases without eyelashes; (b) and (d) are for cases with eyelashes. (Online version in colour.)

Table 4. Eyelash parameters and boundary conditions for different cases.

case type	inlet direction	dimensionless length (L_{mean}/W_x)	orientation
case 1	normal	0.36	upright
case 2	Parallel 1, Parallel 2	0.36	upright
others	normal	0, 0.05, 0.1, 0.15, 0.2, 0.25, 0.3, 0.4, 0.6, 0.8, 1	upright
		0, 0.05, 0.1, 0.15, 0.2, 0.25, 0.3, 0.4, 0.6, 0.8, 1	inward
		0, 0.05, 0.1, 0.15, 0.2, 0.25, 0.3, 0.4, 0.6, 0.8, 1	outward
	Paralle1, Parallel 2	0, 0.05, 0.1, 0.15, 0.2, 0.25, 0.3, 0.4, 0.6, 0.8, 1	upright
		0, 0.05, 0.1, 0.15, 0.2, 0.25, 0.3, 0.4, 0.6, 0.8, 1	inward
		0, 0.05, 0.1, 0.15, 0.2, 0.25, 0.3, 0.4, 0.6, 0.8, 1	outward
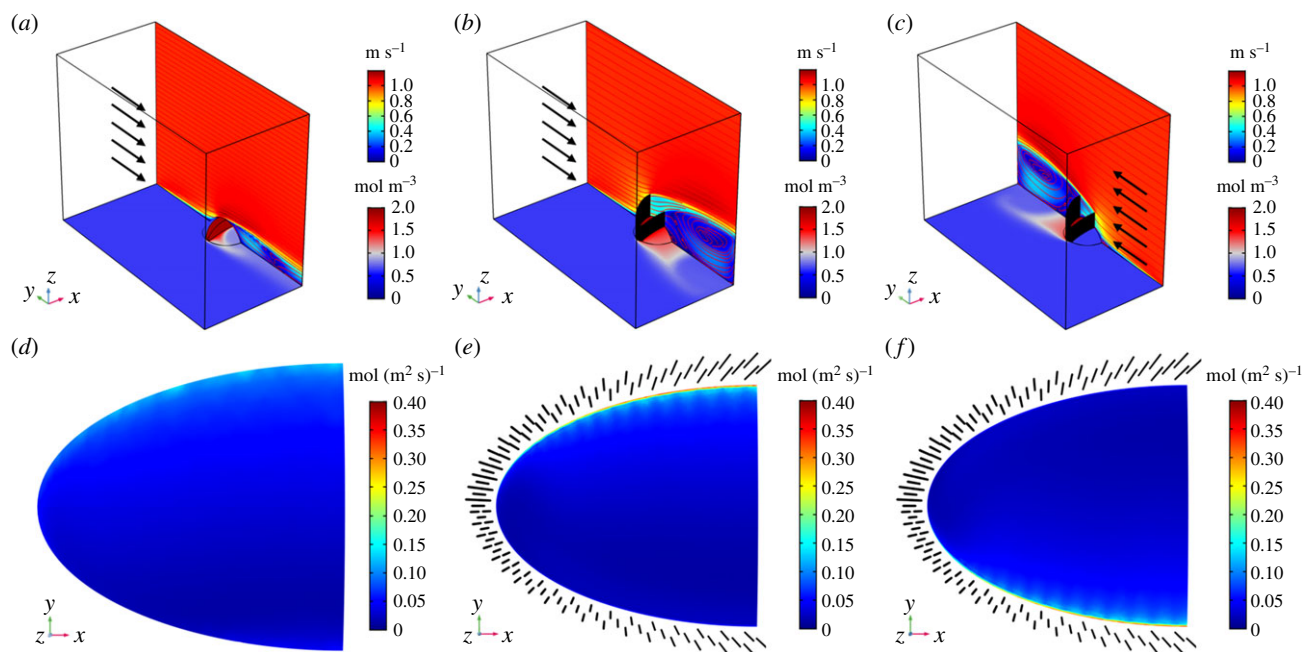
Figure 6. Distributions of physical quantities for the cases with parallel inlet air: (a–c) velocity and vapour concentration distributions; (d–f) vapour flux distributions on the ocular surface; (a) and (d) are for cases without eyelashes, others are for cases with eyelashes. (Online version in colour.)

The results in figure 5a,b show the velocity field with stream lines on the symmetrical plane, and vapour concentration distributions on the bottom surface for case 1. In the case without eyelashes, a dome-shaped low-velocity zone is formed after the inlet air impacting on the eye and face. Symmetrical streamlines can be observed (figure 5a). The water vapour diffuses radially from the ocular surface to the surrounding environment, and the vapour flux on the ocular surface is relatively uniform (figure 5c). Nevertheless, when eyelashes are considered, velocity, vapour concentration and especially vapour flux distributions in the computational domain become quite different. Figure 5b shows that the airflow path is distorted by the eyelashes, and the low-velocity zone becomes more prominent and is extended to the place further away from the eye. When compared with the case without eyelashes, vapour flux decreases dramatically in the central area and increases significantly in the outer rim of the ocular surface. As a consequence, a much less uniform distribution can be observed (figure 5c,d). Thus, the introduction of eyelashes inhibits evaporation over the majority of the ocular surface expect for the rim area. The high vapour flux in the rim area can be mainly attributed to the narrow channels formed by densely arranged eyelashes that can offer high-velocity locations and lead to high rate of vapour removal from the ocular surface. It is also found that, in this specific case, the vapour flux reduction in the central area of the ocular surface leads to a reduction in overall evaporation rate from the ocular surface by 8.01%, indicating the evaporation inhibition function of eyelashes.

Similar plots are given for case 2, where the inlet air flows parallel to the ocular surface (see the streamlines in figure 6a) and all the other conditions are the same as those for case 1. Compared with the case with normal inlet air (figure 5a), the dome-shaped low-velocity zone disappears (figure 6a), which leads to a thinner boundary layer and higher vapour flux from the ocular surface. As shown in figure 6d, larger vapour flux can be identified at an upstream location, where the air starts to impact on the eye. The boundary layer gradually grows along the flow direction, resulting

in a decreasing trend of evaporation flux (figure 6d). With eyelashes taken into account, the airflow is obstructed by the matrix of eyelashes, significant changes can be observed for the flow field (figure 6b,c). The low-velocity zone is formed above the ocular surface and is extended to almost the whole downstream, which results in thicker boundary layers and the decrease in evaporation flux over the majority area of the ocular surface (figure 6e,f). Compared to the case of no eyelashes, the vapour flux decreases 17.79% and 16.45%, respectively, for Parallel 1 and Parallel 2 cases.

Inlet air direction does affect evaporation. Comparing the cases with normal inlet air (case 1) and parallel inlet air (case 2), a larger evaporation rate has been observed for the parallel inlet air (58.39% higher for the case without eyelashes and 41.55% and 43.85% higher for Parallel 1 and Parallel 2 with $L_{mean} = 10$ mm eyelashes). This counterintuitive finding can be clearly explained based on the comprehensive data of velocity and concentration fields discussed above. The cases with parallel inlet air offer higher velocity gradients above the ocular surface, which lead to thinner boundary layers and hence stronger evaporation.

3.2. The effects of eyelash length and orientation on water evaporation

The parametric analyses have been carried out to investigate how the geometry of eyelashes can affect water evaporation on the ocular surface. Two key parameters studied are eyelash length and orientation. Similarly, the numerical simulations are divided into two groups with two different inlet air directions. The detailed settings are listed in table 4.

The dimensionless eyelash length is defined as the ratio between the mean eyelash length (L_{mean}) and palpebral fissure width (W_x). Three eyelash orientations are considered, i.e. upright, inward and outward (figure 7). For each flow direction and each eyelash orientation, 12 different eyelash lengths are studied, which are $L_{mean}/W_x = 0$, 0.05, 0.1, 0.15,
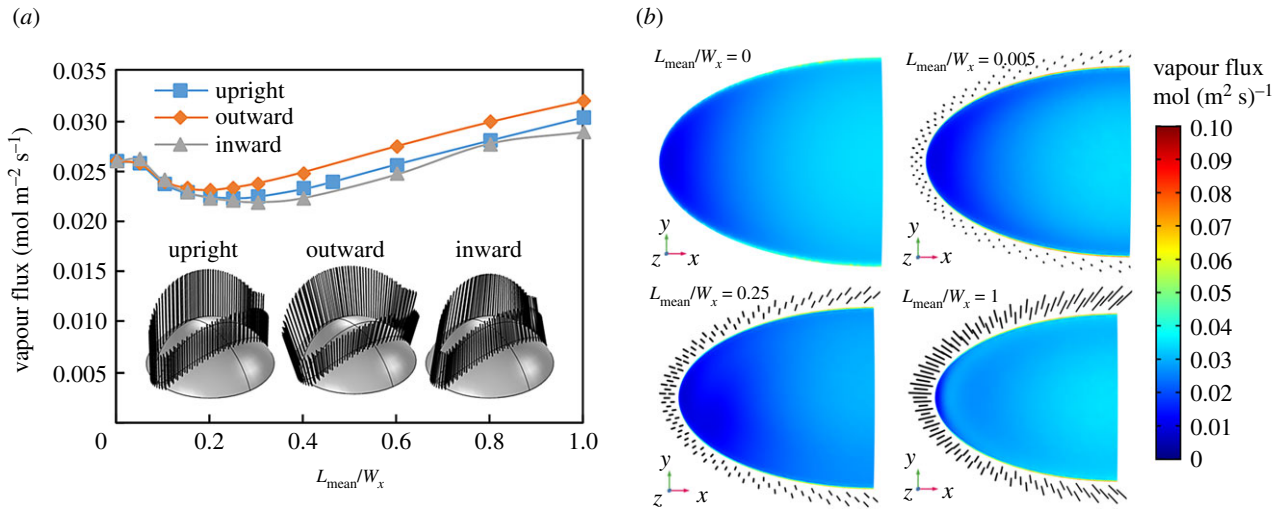
Figure 7. Ocular water evaporation with normal inlet air: (a) evaporation flux as a function of the eyelash length under different eyelash orientations; (b) the vapour flux distribution on the ocular surface with different lengths of upright eyelashes. (Online version in colour.)

0.2, 0.25, 0.3, 0.4, 0.46, 0.6, 0.8 and 1. Among them, 0.46 is the value of the base cases discussed in the previous section.

Figure 7a gives the average evaporation flux on the ocular surface as a function of dimensionless eyelash length for the cases with normal inlet air. The increase in eyelash length leads to the reduction in evaporation rate first, and then an increasing trend can be observed. An optimal eyelash length can be identified, which offers the minimum evaporation flux. Figure 7b indicates vapour flux distributions on the ocular surface with different lengths of upright eyelashes. Comparing with the case of $L_{mean}/W_x = 0$, the vapour flux adjacent to eyelashes decreases in the case of $L_{mean}/W_x = 0.05$, but remains almost the same in the central area of the ocular surface. As the eyelash length increases, the reduction in evaporation in the rim area close to the eyelash (especially the area close to the endpoint of the eye) becomes more significant until the optimal eyelash length is reached, which is about $L_{mean}/W_x = 0.25$. After that, further increase in eyelash length leads to the increase in evaporation in almost the whole ocular surface. It is worthwhile to point out that the evaporation flux of the case with long eyelashes can be even larger than the case without eyelashes (figure 7). Under the condition of normal inlet air, long eyelashes promote (rather than inhibiting) evaporation from the ocular surface, and the rim area adjacent to eyelashes has the highest evaporation rate.

For the case with parallel inlet air, figure 8a,c indicates that, as the eyelash length increases, the average evaporation flux first decreases and then increases slightly (i.e. a minimum evaporation rate exists at an optimal eyelash length of around $L_{mean}/W_x = 0.1$ for Parallel 1 and $L_{mean}/W_x = 0.15$ for Parallel 2). This trend is the same as that in the case with normal inlet air. As shown in figure 8b,d, the evaporation rate gradually decreases along y direction (i.e. the inlet air direction), implying that most evaporation occurs in the upstream area. Increasing eyelash length from $L_{mean}/W_x = 0$ to optimal eyelash length inhibits evaporation both in the downstream area (see the darker colour) and the upstream area (see the narrower high-flux zone). Further increase in eyelash length leads to the enhanced evaporation in the upstream area.

Regardless of inlet air direction, the existence of eyelash changes airflow patterns around the ocular surface. It affects the thickness distribution of the velocity boundary layer and hence the concentration boundary layer. As a direct consequence, the evaporation flux demonstrates different distributions under different eyelash lengths. Taking a close look at velocity and boundary layers can offer an in-depth understanding of the protection mechanism of eyelashes.

Figures 7 and 8 indicate that the rim area of the ocular surface has the highest evaporation flux. The velocity profiles in the rim area close to eyelashes are plotted in figure 9 for further analyses. The sizes of arrows in all subplots of figure 9 are proportional to the velocity magnitude. The velocity gradient can be clearly identified, which is a quantitative indicator of the thickness of velocity boundary layer. A higher velocity gradient indicates a thinner boundary layer, implying that evaporated moisture can be taken away by the ambient air more easily, leading to a larger evaporation rate. When the eyelashes are short ($L_{mean}/W_x = 0.05$), the flow pattern is very similar to the case without eyelashes (the case with the first type of parallel inlet air). The velocity gradient becomes much lower when the eyelash length reaches the optimal eyelash length, implying a much thicker boundary layer. After that, the velocity as well as its gradient above the ocular surface gradually increase and the boundary layer becomes thinner. These phenomena can be observed for both cases with different inlet directions. The velocity profile information can be used to explain the trend of evaporation as a function of the eyelash length (see figures 7 and 8). In general, the velocity gradient for the case with parallel inlet air is larger than that with normal inlet air, which is especially true when the eyelash length is short ($L_{mean}/W_x <$ the optimal eyelash length, figure 9). Thus, a thinner boundary layer and a higher evaporation rate are expected for the case with parallel inlet air. It can be evidenced by the data in figures 7 and 8.

The thickness of the velocity boundary layer is only an indirect indicator of evaporation rate. The concentration boundary layer, however, is a more straightforward and convincing indicator of the evaporation rate. A thinner concentration boundary layer offers a higher concentration gradient and thus a higher evaporation flux. In order to compare the thickness of concentration boundary layers above the ocular surface, vapour concentrations along cutlines adjacent to the eyelash have been plotted in figure 10. For a certain
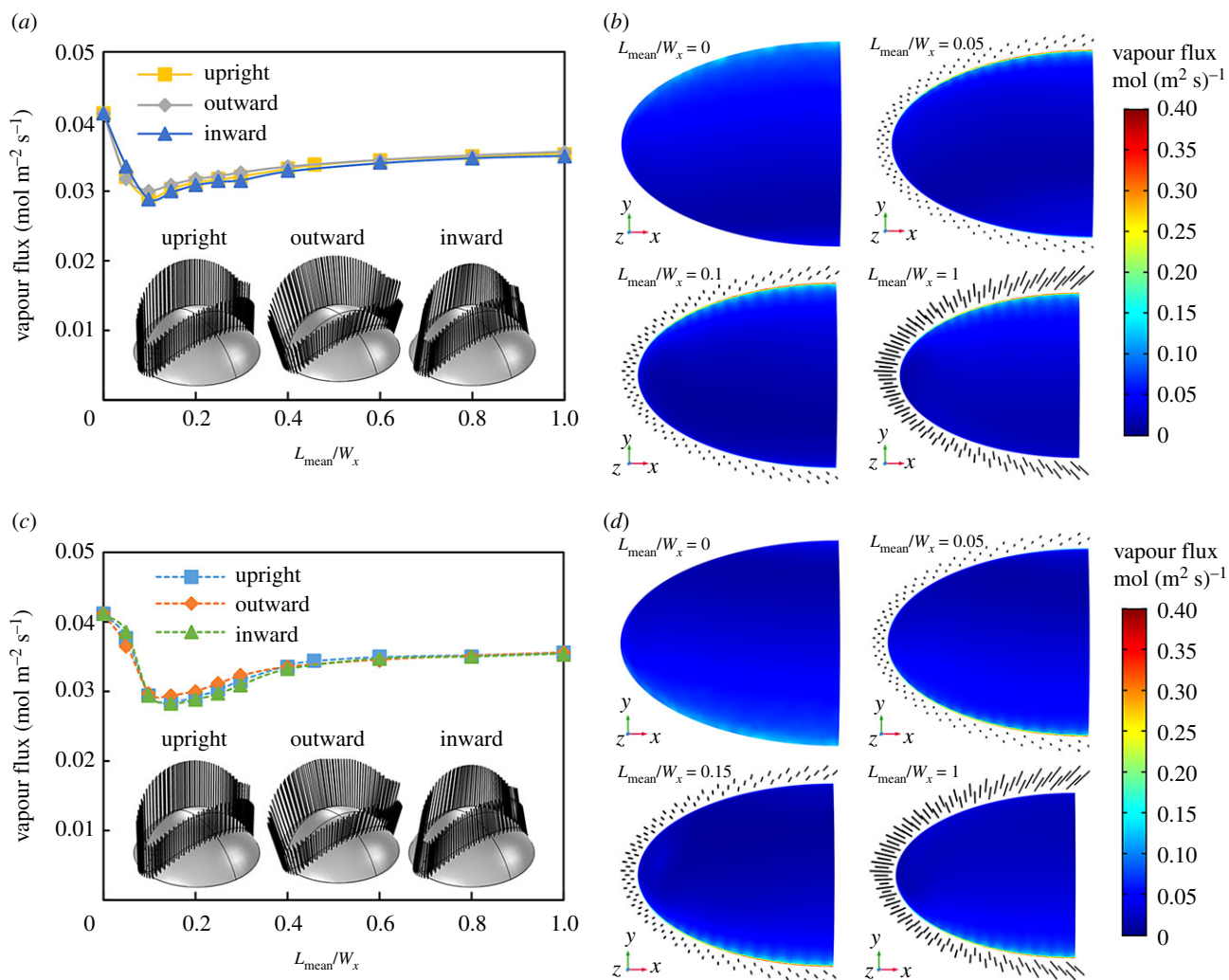
Figure 8. Ocular water evaporation with parallel inlet air: (a,c) evaporation flux as a function of the eyelash length under different eyelash orientations for two different parallel inlet conditions; (b,d) the vapour flux distribution on the ocular surface with different lengths of upright eyelashes for two different parallel inlet conditions. (Online version in colour.)
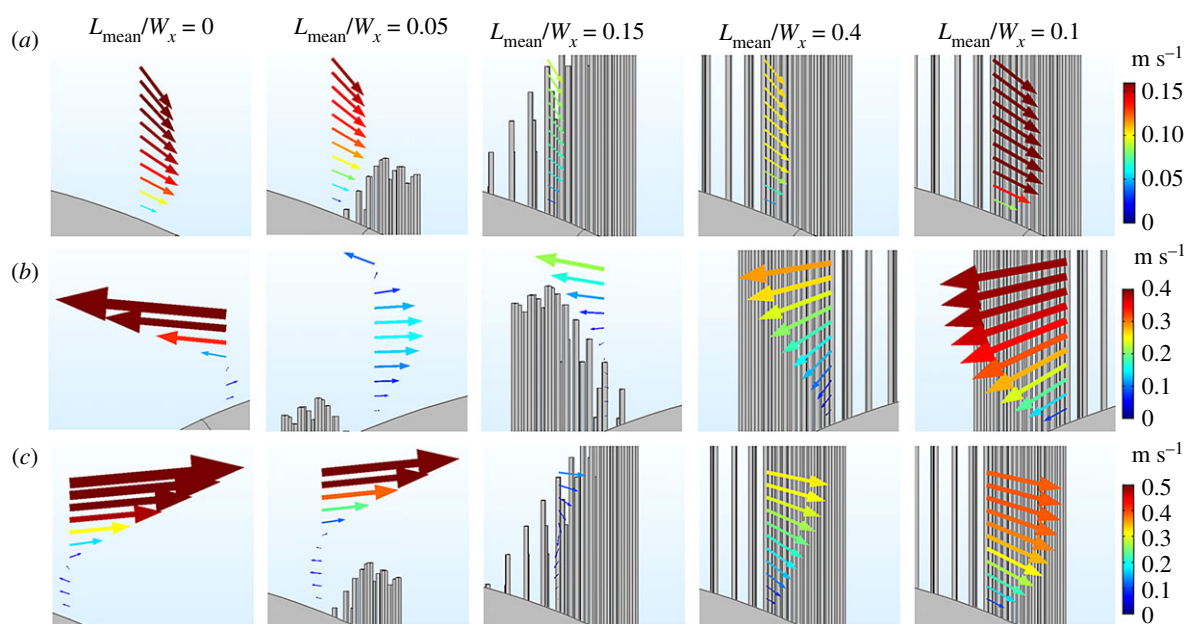
Figure 9. The velocity profiles close to the eyelash for: (a) the case with normal inlet air, (b) the case with the first type of parallel inlet air (downstream) and (c) the case with the second type of parallel inlet air (downstream). In each row, the length of the arrow is proportional to the velocity magnitude, whose maximum and minimum values are indicated by the colour bar. (Online version in colour.)
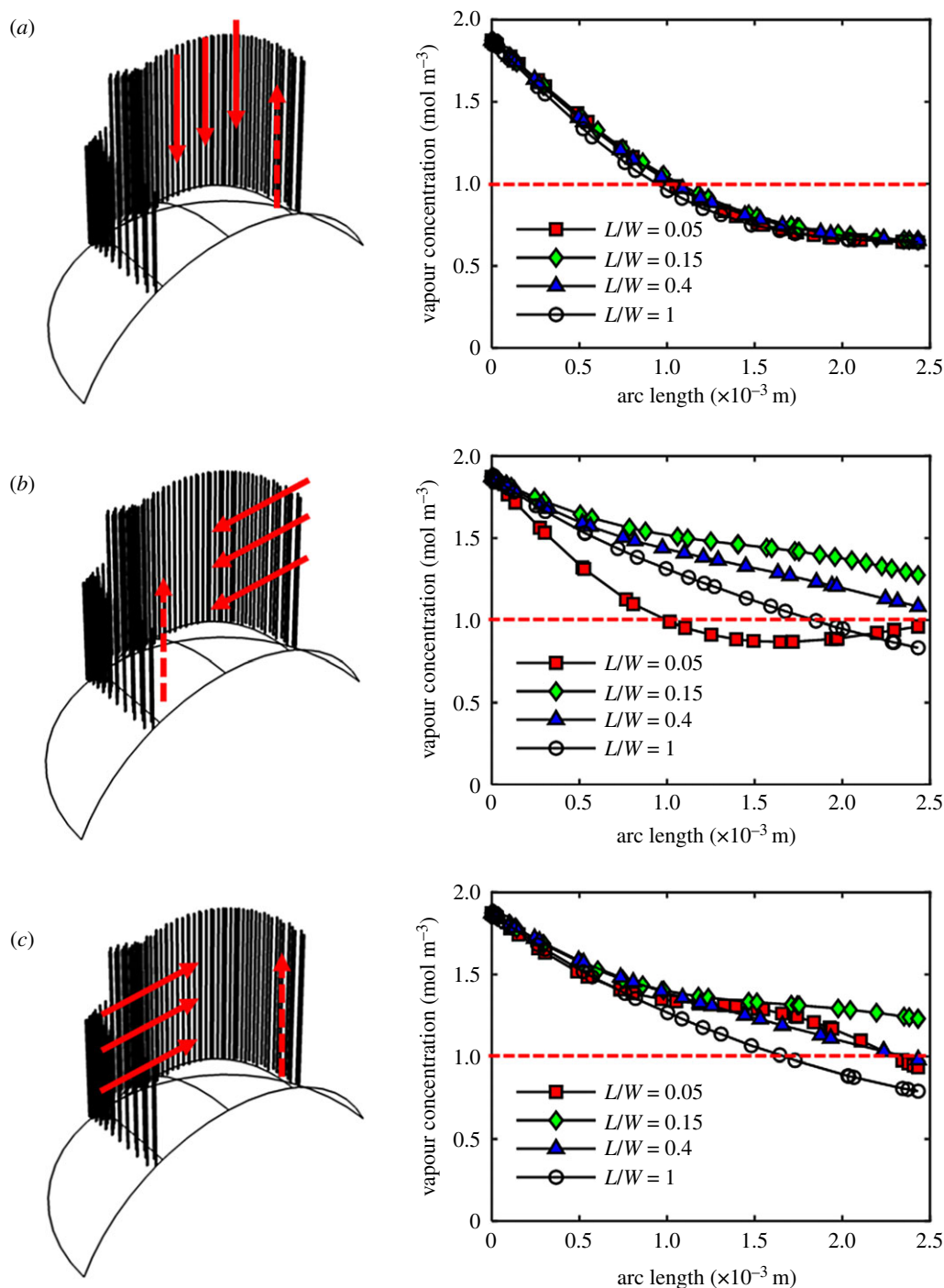
Figure 10. The vapour concentration distributions along cutlines under different lengths of upright eyelashes (i.e. L_{mean}/W_x = 0.05, 0.15, 0.4 and 1) for: (a) the case with normal inlet air, (b) the case with Parallel 1 inlet air (downstream) and (c) the case with Parallel 2 inlet air (downstream). (Online version in colour.)

concentration (e.g. 1 mol m^{-3} plotted in figure 10) that is close to the bulk concentration, the longer the arc length, the thicker the concentration boundary layer is. As expected, regardless of the inlet air direction, the optimal eyelash length offers the thickest boundary layer, and hence the lowest evaporation rate. The data also show that the boundary layer is thickened when the dimensionless eyelash length increases from 0.05 to the optimal eyelash length. Further increase in eyelash length, however, leads to the decrease in boundary layer thickness (figure 10). It explains the trend identified in figures 7a and 8a,c. In summary, the thickness of concentration boundary layer can be used to interpret the evaporation rate. The boundary layer can be effectively thickened through increasing eyelash length when eyelashes are relatively short, which behave as obstacles to moisture removal. However, long

eyelashes behave like channels that can effectively direct air flow towards/away from the ocular surface, and hence can promote moisture removal and evaporation.

Considering the individual differences of human beings, various eyelash orientations including upright, inward and outward are also studied in this work. The effects of eyelash orientation on evaporation flux have been demonstrated in figures 7 and 8. Three orientations show the same trend. An optimal eyelash length can be observed for all orientations. Thus, eyelash orientation does not lead to great influence on evaporation.

4. Conclusion

In the present work, a multi-physics model has been developed to simulate and predict water evaporation from the

human ocular surface under the influence of eyelashes. The momentum, heat and mass transfer models have been fully coupled with the evaporation model. A series of numerical experiments are designed to investigate the effect of human eyelashes on ocular water evaporation considering the realistic structures of eyelashes.

Comparisons between the cases without eyelashes and with eyelashes length of 10 mm reveal the protective function of eyelashes on human eyes in terms of evaporation inhibition. The effects of inlet air direction, eyelash length and orientation have been systematically carried out. Results show a counterintuitive finding, i.e. parallel inlet air causes a high evaporation flux when compared with the case with normal inlet air. Regardless of inlet air direction, with the increase in eyelash length, the evaporation flux decreases first and then increases. Although various eyelash orientations produce some minor differences, eyelash orientations have no obvious effect on evaporation protection and the optimal eyelash length has been observed in all three eyelash orientations. Specifically, in the cases with normal inlet air and upright eyelashes, optimal eyelashes can reduce nearly 14.11% evaporation when compared with the case without eyelashes. The reduction percentage becomes 11.17% and 15.48% for outward and inward eyelashes, respectively. In the cases with parallel inlet air, the reduction rates are almost two to three times that of the case with normal inlet, which are 28.98%, 26.64% and 29.57%, respectively, for upright, outward and inward eyelashes in Parallel 1. The corresponding values are 30.61%, 28.16% and 31.17% in Parallel 2. Eyelashes shorter than the optimal length function as obstacles to moisture removal, while those long ones form channels that can direct air flow and promote moisture removal. These findings have been explained through analyses of velocity and concentration boundary layers under different conditions. Furthermore, the distributions of evaporation flux on the ocular surface have been revealed. For the case with normal inlet air, the rim area of the ocular surface close to eyelashes has a higher evaporation rate when compared with the central area. For the case with parallel inlet air, the upstream area of the ocular surface dominates the overall evaporation. These new findings advance our understanding of the protective behaviour of human eyelashes.

Multi-physics models established in this work offer great opportunities to study tear film evaporation under different scenarios in the future. To name one example, the effects of air temperature and humidity on tear film evaporation can help us understand the differences of eyelashes between animals living in drastic different weather conditions. The main phenomenon focused in the current study is water evaporation on the ocular surface. Thus, the optimal eyelash length obtained in this work is only for water evaporation protection. In reality, the eyelashes are multifunctional, e.g. sunlight and dust protection. This can explain why real human eyelashes are longer than the optimal value identified in this work. Therefore, particle flying and deposition behaviour around the ocular surface is also an interesting phenomenon worth further investigation in the future. In addition, the eyelashes used in current simulations are straight. But the realistic eyelashes are slightly curved, the curvature of false eyelashes for makeup are more obvious. Hence, research regarding the influence of the curvature of eyelashes on water evaporation from the ocular surface is valuable and will be investigated in the future. In summary, this work has provided the basis for further complicated studies and applications involving eyelash-inspired systems.

References

1. Delaplace G, Gu Y, Liu M, Jeantet R, Xiao J, Chen XD. 2018 Homogenization of liquids inside a new soft elastic reactor: revealing mixing behavior through dimensional analysis. *Chem. Eng. Sci.* **192**, 1071–1080. (doi:10.1016/j.ces.2018.08.023)

2. Gao Q, Xiao J, Chen XD. 2016 Understanding hydrotropism: a chemical engineering perspective. *AIChE J.* **62**, 1331–1346. (doi:10.1002/aic.15110)

3. Li C, Xiao J, Zhang Y, Chen XD. 2019 Mixing in a soft-elastic reactor (SER): a simulation study. *Can. J. Chem. Eng.* **97**, 676–686. (doi:10.1002/cjce.23351)

4. Liu M, Xiao J, Chen XD. 2018 A soft-elastic reactor inspired by the animal upper digestion tract. *Chem. Eng. Technol.* **41**, 1051–1056. (doi:10.1002/ceat.201600617)

5. Shapiro OH, Fernandez VI, Garren M, Guasto JS, Debaillon-Vesque FP, Kramarsky-Winter E, Vardi A, Stocker R. 2014 Vortical ciliary flows actively enhance mass transport in reef corals. *Proc. Natl Acad. Sci. USA* **111**, 13 391–13 396. (doi:10.1073/pnas.1323094111)

6. Xiao J, Zou C, Liu M, Zhang G, Delaplace G, Jeantet R, Chen XD. 2018 Mixing in a soft-elastic reactor (SER) characterized using an RGB based image analysis method. *Chem. Eng. Sci.* **181**, 272–285. (doi:10.1016/j.ces.2018.02.019)

7. Amador GJ, Mao W, DeMercurio P, Montero C, Clewis J, Alexeev A, Hu DL. 2015 Eyelashes divert airflow to protect the eye. *J. R. Soc. Interface* **12**, 20141294. (doi:10.1098/rsif.2014.1294)

8. Gong S, Zhou Q, LeDoux MS. 2003 Blink-related sensorimotor anatomy in the rat. *Anat. Embryol.* **207**, 193–208. (doi:10.1007/s00429-003-0341-6)

9. Martin GR, Coetzee HC. 2004 Visual fields in hornbills: precision-grasping and sunshades. *Ibis* **146**, 18–26. (doi:10.1111/j.1474-919X.2004.00211.x)

10. Cohn JF, Xiao J, Moriyama T, Ambadar Z, Kanade T. 2003 Automatic recognition of eye blinking in spontaneously occurring behavior. *Behav. Res. Methods Instrum. Comput.* **35**, 420–428. (doi:10.3758/BF03195519)

11. Johnstone MA, Albert DM. 2002 Prostaglandin-induced hair growth. *Surv. Ophthalmol.* **47**, S185–S202. (doi:10.1016/S0039-6257(02)00307-7)

12. Levy Y, Segal N, Ben-Amitai D, Danon Y. 2004 Eyelash length in children and adolescents with allergic diseases. *Pediatr. Dermatol.* **21**, 534–537. (doi:10.1111/j.0736-8046.2004.21501.x)

13. Amador GJ, Durand F, Mao W, Pusulri S, Takahashi H, Nguyen V-T, Shimoyama I, Alexeev A, Hu DL. 2015 Insects have hairy eyes that reduce particle

deposition. *Eur. Phys. J. Spec. Top.* **224**, 3361–3377. (doi:10.1140/epjst/e2015-50094-x)

14. Thibaut S, De Becker E, Caisey L, Baras D, Karatas S, Jammayrac O, Pisella P, Bernard B. 2010 Human eyelash characterization. *Br. J. Dermatol.* **162**, 304–310. (doi:10.1111/j.1365-2133.2009.09487.x)

15. Netter FH. 2018 *Atlas of human anatomy*, 7 edn. New York, NY: Elsevier.

16. Standring S. 2015 *Gray's anatomy international edition: the anatomical basis of clinical practice*, 41 edn. New York, NY: Elsevier Health Sciences.

17. Read SA, Collins MJ, Carney LG. 2006 The morphology of the palpebral fissure in different directions of vertical gaze. *Optom. Vis. Sci.* **83**, 715–722. (doi:10.1097/01.opx.0000236811.78177.97)

18. Diao Y, Leung SW, He Y, Sun W, Chan KH, Siu YM, Kong R. 2016 Detailed modeling of palpebral fissure and its influence on SAR and temperature rise in human eye under GHz exposures.

Bioelectromagnetics **37**, 256–263. (doi:10.1002/bem.21973)

19. Vasanthakumar P, Kumar P, Rao M. 2013 Anthropometric analysis of palpebral fissure dimensions and its position in South Indian ethnic adults. *Oman Med. J.* **28**, 26. (doi:10.5001/omj.2013.06)

20. Procianoy F, Mendonça TB, Bins CA, Lang MP. 2015 Characterization of normal mediolateral angular direction of lower eyelid eyelashes in different age groups. *Ophthal. Plast. Reconstr. Surg.* **31**, 332–333. (doi:10.1097/IOP.0000000000000473)

21. Tohmyoh H, Ishihara M, Ikuta K, Watanabe T. 2018 On the correlation between the curvature of the human eyelash and its geometrical features. *Acta Biomater.* **76**, 108–115. (doi:10.1016/j.actbio.2018.07.005)

22. Terada O, Chiba K, Senoo T, Obara Y. 2004 Ocular surface temperature of meibomia gland dysfunction patients and the melting point of meibomian gland

secretions. *Nippon Ganka Gakkai Zasshi* **108**, 690–693.

23. Khong J, Casson R, Huilgol S, Selva D. 2006 Madarosis. *Surv. Ophthalmol.* **51**, 550–560. (doi:10.1016/j.survophthal.2006.08.004)

24. Kundu PK, Cohen IM, Dowling DR. 2015 *Fluid mechanics*, 6th edn. New York, NY: Elsevier.

25. Perry RH, Green DW. 2007 *Perry's chemical engineer's handbook*, 8 edn. New York, NY: McGraw-Hill.

26. Alduchov OA, Eskridge RE. 1996 Improved Magnus form approximation of saturation vapor pressure. *J. Appl. Meteorol.* **35**, 601–609. (doi:10.1175/1520-0450(1996)035<0601:IMFAOS>2.0.CO;2)

27. Patel K, Chen XD, Jeantet R, Schuck P. 2010 One-dimensional simulation of co-current, dairy spray drying systems—pros and cons. *Dairy Sci. Technol.* **90**, 181–210. (doi:10.1051/dst/2009059)

28. COMSOL Multiphysics® v. 5.4. 2019 www.comsol.com. Stockholm, Sweden: COMSOL AB.